



On the effect of strand damage on the operating margin of a Nb₃Sn Rutherford cable

G. Succi^{a,*}, L. Bottura^a, M. Breschi^b, B. Bordini^a, D. Baffari^a

^a CERN, The European Laboratory for Particle Physics, Switzerland

^b The University of Bologna, Italy

ABSTRACT

Degradation of performance in superconducting magnets can be a major concern when a brittle material like Nb₃Sn is employed. Indeed, degradation can significantly alter the transport properties of a cable if, e.g. an excessive stress is applied during coil and magnet manufacturing. In this paper, we study the limiting case of a strand in a Rutherford type cable that, at a given location, does not carry any current. We refer to such strand simplistically as the 'broken strand', regardless of the actual cause disrupting the current carrying capability. To this aim, a model was developed using the code THEA, to describe the electric and thermal properties of the Rutherford cable of the HL-LHC 11 T dipole magnet. First, we studied the current distribution in the cable, considering a uniform current in each strand at the boundaries, namely with single strands behaving as current generators, or zero-resistance joints, namely equipotential boundaries. We concluded that the two adjacent strands to the broken strand play the most significant role in the distribution of current out of the broken strand. A similar situation was found when a strand of the cable suddenly goes normal, i.e. it quenches. We then derived the characteristic times and lengths for the current redistribution in the case of an instantaneous strand breakage. We describe in detail the procedure to extract such quantities from the simulation results, and we demonstrate a good agreement between the numerically derived characteristic times and the analytical calculation from a previous theoretical work. The results of this study help to shed light on the repercussions of degradation in brittle materials such as Nb₃Sn. This subject is indeed crucial for the next generation of accelerator coils and magnets for high-energy physics projects.

1. Introduction

Current distribution and redistribution in multi-strand superconducting cables is one of the phenomena that is known to affect the operating margin [1], stable performance [2] and field quality [3,4] of particle accelerator magnets. It is a generally accepted common wisdom that a uniform current distribution in a cable is always the preferable situation, although a current non-uniformity does not necessarily lead to premature quench. This depends on several strand and cable parameters, such as the cable geometry and length, electrical, thermal and cooling characteristics, distribution of critical current within the cable, localized or distributed degradation, joint resistance, and so on.

To reduce the uncertainty originating by the complexity of current distribution and redistribution phenomena, strands in superconducting cables for fusion and accelerator magnet applications are twisted and partially, or fully, transposed. In particular, *transposition* is of paramount importance since it limits the coupling currents generated when the cable is exposed to a time-varying external magnetic field, thus achieving a current distribution as uniform as possible. In spite of this, the deviation from the ideal situation of an infinitely long cable,

perfectly transposed, in a perfectly homogeneous field, always results in an inductive imbalance between strands and a difference among the currents carried by each strand of the cable. A certain degree of non-uniformity is hence always present in cables because of the *inductive* drive during ramps, although not always of large amplitude. In addition, whenever the strands in the cable have a longitudinal resistance distribution, e.g. locally degraded critical properties or non-homogeneous joint resistance, the longitudinal voltage drives a current redistribution in the cable. We can call this a *resistive* source of non-uniform current distribution.

The subject of current distribution in its various origins and effects is complex, and it has been studied extensively from many perspectives during the past forty years [5–36]. We are revisiting this matter in the scope of the analysis of production and performance of the Nb₃Sn magnets for the High Luminosity upgrade of the Large Hadron Collider at CERN (HL-LHC). We recall that the main objective of the HL-LHC project is to increase the nominal LHC luminosity by an order of magnitude [37], and this requires a number of dipoles and quadrupoles [38,39] with higher performance than the present LHC magnets. In particular, the project foresees to install a total of sixteen MQXF

* Corresponding author.

E-mail address: giovanni.succi@cern.ch (G. Succi).

<https://doi.org/10.1016/j.cryogenics.2022.103458>

Received 9 December 2021; Received in revised form 16 March 2022; Accepted 4 April 2022

Available online 28 May 2022

0011-2275/© 2022 The Authors. Published by Elsevier Ltd. This is an open access article under the CC BY license (<http://creativecommons.org/licenses/by/4.0/>).

quadrupole magnets at the ATLAS and CMS Interaction Points (four magnets per side). Moreover, additional beam collimators will be required. The space for such collimators will be obtained by substituting two full-length 15 m LHC dipoles, having a bore field of 8.33 T, with a set of four shorter dipoles producing a bore field of 11 T. This is why Nb_3Sn was selected profiting from better superconducting properties compared to the $Nb-Ti$ used in the LHC.

Nb_3Sn , however, is brittle and it is well known that excessive stress and strain may result in conductor damage [44–49], thus leading to a resistive-driven non-homogeneous current distribution. Proper engineering margins are applied to prevent this from happening. Still, the delicate manufacturing process of the Wind-and-React HL-LHC Nb_3Sn magnets, and the challenging and complex electro- and thermo-mechanical operating conditions are such that local degradation may occasionally happen. In this paper, we study the effect of localized conductor damage, without entering in the details of the degradation origin and mechanism, but rather focussing on the features of the resulting current distribution and redistribution, and the potential impact on magnet performance. We are particularly interested to see whether degradation of a single strand can be accommodated by the rest of the cable, or conversely if it has significant impact on performance. We refer colloquially to the single strand with degraded performance as *broken strand*.

Among the many studies on current distribution and redistribution, we have selected a sample of previous work that is directly relevant to the issue we wish to address. Specifically, Turck [5] stressed the importance of wire transposition for the operation of pulsed coils and proposed an analytical method to derive the current distribution in a pair of non-insulated, magnetically coupled wires subjected to a local breakage in one strand. He proved that the intact wire carries the totality of the current in the broken spot and that the discharge of the broken wire propagates from such spot by means of a diffusion mechanism, eventually leaving the broken wire without current.

Ries [6] considered the transition of a single wire to the normal state in a two-wire system, conceptually similar to a local damage. In particular, he showed analytical expressions for the current and voltage diffusion from the normal and the superconducting region of a quenched strand to the adjacent fully superconducting strand. He also provided an estimation of the corresponding Joule losses and of their decay in time.

Experimental work has been conducted in this sense, as well. Two groups, Faivre and Turck [7] and Knoopers, ten Kate, and van de Klundert [8] independently, built a six-strand twisted cable, which was then subjected to both alternating current (AC) and direct current (DC). Results from the two groups were similar, and indicated that the current is always distributed non-uniformly among the strands with differences in the order of 10 %, despite the efforts to obtain an equal resistance at the cable ends. Furthermore, both groups observed that a quench in one strand caused the current to redistribute almost exclusively into the immediate neighbour strands, thus reducing the maximum current carried by the whole cable.

The above studies [5,6] make extensive use of closed-form analytical solutions, and cannot be easily extended to the complex geometry and characteristics of a multi-strand cable. First attempts to describe the current distribution in multi-strand Rutherford cable were thus conducted by means of discrete network models [9–11]. The model represents each current loop of the cable and shows that in a perfectly transposed cable the coupling currents in response to a homogeneous varying magnetic field are periodic with a period equal to the cable pitch length. In presence of transposition errors, additional screening currents flow over a large portion of the cable and are superimposed to the short-range coupling currents [12–14]. A similar approach was followed for cable-in-conduit-conductors (CICCs) for fusion experiments in [15–17], leading to a qualitative understanding of the effect of strand damage on the performance of ITER conductor samples [49–52]. Despite its precision, the number of variables in a network model increases dramatically with the cable length, which does not make it suitable for computations

on very long cables, such as the situation in coils.

Modelling based on a set of partial differential equations to solve the electrical network of the Rutherford cable in 1-D, an extension of the original analytical methods of [5] and [6], was proposed in [18,19]. This approach uses a continuous transverse conductance for the contact between strands, and can be detailed to the level of a single strand (one differential equation per strand) where the current is assumed to be uniform over a strand cross section.

The structure of the equations is suitable for the analysis of long cable lengths and allows efficient coupling with the thermal and hydraulic models to compute the full thermal, hydraulic and electric evolution of the cable state. Again, a similar approach was developed for CICCs, see [20–24]. The particularity of the Rutherford cables considered in our study, besides their regular geometry, is that their stability is much lower than CICCs', implying that non-homogeneous current distribution can have a more deleterious effect.

The continuum representation of the electrical network was used in [25] to evaluate the long-range eddy currents generated by time-dependent magnetic fields applied to a Rutherford cable. Particular emphasis was put in the derivation of the model parameters, such as strand inductance and inter-strand conductance, as they were found critical to properly model the network. A simplified approach where strands were grouped into so-called 'superstrands' to reduce model complexity was also adopted in [26].

Finally, we recall that the continuum formulation for an N -strand cable was solved analytically in [27] under specific symmetric and periodicity conditions on the matrices of inductance and conductance. The solution is quite general and describes the current evolution under every source of current imbalance, such as initial conditions or external voltage perturbations. The same work provides an analytical expression for the time constants associated with the eigen-modes of the system. As we will discuss later, the time constants are of great relevance for the scope of the present work.

In the context of this study, we wish to model the current distribution and associated performance limits of the full-size, 40-strand cable for the 11 T dipole magnet, as representative of the Nb_3Sn cable developed for the HL-LHC project. The MQXF cable has larger strand but essentially identical configuration and we expect electrical properties to be similar. Our results on the study of the 11 T cable can hence be transposed nearly directly to the MQXF cable. We consider position- and time-dependent field and critical properties, including the effect of Joule heat in proximity of the critical surface, and considering local strand degradation, i. e. a *broken strand*. To this end we have selected the model implemented in THEA [28] developed in the early 2000s to widen the analysis spectrum and to address problems related to the design and analysis of superconducting magnets. The studies conducted in [27] and [29–30] show that the code has the required capability.

In Section 2 we describe the model developed using the features offered by the THEA code. We then give in Section 3 the nominal cable geometry and characteristics selected for the simulation, based on the HL-LHC 11 T dipole [38]. Section 4 reports the main results of the simulations performed and in particular the derivation of the characteristic times and lengths of the system which are relevant to evaluate the impact of a broken strand in a Nb_3Sn Rutherford cable of the class considered. Section 5 contains the conclusion.

2. General features of the THEA model

The model implemented in the THEA code is a generic, multi-component and multi-channel model for the analysis of the thermal, hydraulic and electric transients in superconducting cables. It is based on a continuum description of heat transfer, fluid flow and current distribution. Specifically, the longitudinal resistance, transverse conductance and inductance are parameters defined per unit cable length, and they can vary arbitrarily as a function of position and time. The model assumes that the ratio of length to cross sectional dimension

of the cable is very large, and neglects the current and temperature distribution over the cross section of a single strand. In this case, it is possible to write the governing equations of cable temperature, flow and current as a system of 1-D PDEs [18,19]. The parametric implementation of the model allows to consider an arbitrary number of strands in a cable, and thus it is capable of describing much of the 2-D and 3-D complexity of a superconducting cable, as shown below. We limit our discussion to the general features of the electric model that are adapted to describe a Rutherford cable, leaving details on the thermal model and coupling of thermal and electric physics domain to [20–21] and [31].

2.1. Electric modelling

The system of N governing equations for the electrical network (one per strand) is derived applying Kirchhoff's laws on the distributed parameters network and it is typical of diffusion phenomena [31]:

$$\hat{g} \hat{l} \frac{\partial \vec{i}}{\partial t} + \frac{\partial^2 \vec{i}}{\partial x^2} + \hat{g} \hat{r} \vec{i} - \hat{g} \vec{v}^{ext} = 0, \quad (1)$$

where \hat{g} is the $N \times N$ conductance matrix per unit length, \hat{l} is the $N \times N$ inductance matrix per unit length, \hat{r} is the $N \times N$ matrix of the longitudinal resistance of the strands per unit length, \vec{i} is the vector with N components describing the currents in each strand as function of both space and time, and \vec{v}^{ext} is also a vector with N components for the external voltage source coupled to each strand.

2.1.1. Conductance matrix

In the case of a Rutherford cable the conductance matrix is symmetric and circulant (see [31]) and is built as follows:

$$\hat{g} = \begin{bmatrix} 0 & g_a & g_c & & g_c & g_c & g_a \\ g_a & 0 & g_a & \cdots & g_c & g_c & g_c \\ g_c & g_a & 0 & & g_c & g_c & g_c \\ \vdots & & & \ddots & & & \\ g_c & g_c & g_c & & 0 & g_a & g_c \\ g_c & g_c & g_c & \cdots & g_a & 0 & g_a \\ g_a & g_c & g_c & & g_c & g_a & 0 \end{bmatrix} \quad (2)$$

where g_a is the conductance per unit length between two adjacent strands, and g_c is the conductance per unit length between two crossing strands. The structure of \hat{g} reflects the geometrical arrangement of the N strands in a Rutherford cable, where two strands i and j are either adjacent (couples of neighbouring strands with $|i - j|$ equal to 1 or $(N-1)$) or crossing (any other couple of strands).

The inter-strand conductance per unit length can be computed by means of the more commonly used adjacent and crossing contact resistance, according to [31]:

$$\begin{cases} g_a = \frac{1}{R_a} \frac{2(N-1)}{t_p} \\ g_c = \frac{1}{R_c} \frac{2}{t_p} \end{cases} \quad (3)$$

Values of $R_a = 0.5 \mu\Omega$ and $R_c = 180 \mu\Omega$ for adjacent and crossing contact resistances are considered in this work, as discussed in [41], which are similar to those in [42].

Clearly, our model does not take into account the dispersion of contact resistance values along the cable length, nor in the joints. The possibility of a distribution of damage along the cable length, which is another relevant issue, is not addressed as well. We focus here on simplified conditions to progress in the understanding, while avoiding the complex interplay of damage and coupling of strands. Analyses that take into account resistance and damage distributions are reported elsewhere, see [29] and [55].

2.1.2. Inductance matrix

The 3-D shape of the strands in the cable makes an analytical computation of strand inductances impractical. For our work, we have computed self and mutual strand inductances using a 3-D magneto-static calculation software [53], which allows building cables of arbitrary geometry in 3-D, including Rutherford.

In particular, the code divides each strand into *bricks*, for which analytical equations for the vector potential can be used to integrate the inductance matrix of the whole system, brick by brick, and combine it to yield values for each strand. The result is the $N \times N$ inductance matrix \hat{l} .

In an infinitely long cable strands would be inductively equivalent to each other, since they would enclose the same magnetic flux along the length. The corresponding inductance matrix would therefore be circulant. Conversely, in a real cable of finite length the strands are not inductively equivalent because of imperfect transposition. The resulting inductance matrix computed by the above method for a cable of finite length is hence, correctly, non-circulant.

Though this is a physical effect, the objective of our study is to consider equivalent strands to avoid current imbalances due to the intrinsic mathematical description of the system (e.g. a non-circulant matrix). To this end, we have applied a regularization procedure. The inductance matrix was first computed for a 1 m long cable, which already yields a good approximation of a circulant matrix (within 1 %). We used 100 elements to mesh this domain, such that the space-step is 1 element/centimetre and the computation time is limited to a few minutes. We have then taken the entries in the inductance matrix for the first strand, and used them to build a numerically exact circulant matrix. This expedient ensures that the current distribution and redistribution is solely associated with the resistive effects related to the presence of a broken strand, as described later, and not by inductive voltages, with a negligible loss of accuracy.

2.1.3. Longitudinal resistance and voltage sources

The longitudinal resistance \hat{r} is a diagonal $N \times N$ matrix whose entries are the resistances of each strand, zero in full superconducting state. The model for the longitudinal resistance of a superconducting strand uses the temperature- and field-dependent properties of the superconductor [43] and of the stabiliser. The current sharing, when the superconducting strand approaches the critical surface, is computed using a power law for the voltage-current characteristics of the superconductor. This results in the typical soft transition, usually described with the n index ($n = 40$ in our model).

External voltage sources \vec{v}^{ext} are associated with the electromotive forces induced in the strand loops during electrodynamic transients. According to our discussion in the introduction, these are the inductive drivers of voltage distribution and redistribution. In our case, we limit the analysis to the resistive effects, and we therefore neglect them here.

3. Adiabatic model of the 11 T dipole cable

In this work we have taken as reference the cable developed for the 11 T dipole magnet (also referred to as '11 T dipole' in the following). The cable consists of 40 strands twisted into a Rutherford cable configuration with nominal dimensions of 14.7 mm width and 1.25 mm mid-thickness, a keystone angle of 0.7 degrees and a twist pitch of 100 mm, as reported in Table 1.

The Nb_3Sn strands have a diameter of 0.7 mm, a Cu:non-Cu ratio of 1.15 and a minimum RRR of 100. A cable is insulated by a layer of mica, folded as a 'C' around the cable, and kept in place by a glass-fibre braid. The total insulation thickness is 100 μm . The 11 T dipole coils are manufactured using the Wind-and-React technique. First, a unit length of 750 m of insulated cable is wound in a cos-theta configuration. This coil is then heat treated to form the superconducting phase, impregnated with CTD-101 epoxy resin, and cured to cast the brittle strands in a sturdy composite.

Table 1

11 T Cable Model parameters	
Nominal cable current, I_{nom}	11.85 kA
Number of strands, N	40
Average current per strand, I_{nom}/N	296.25 A
Critical current of a strand, $I_{s,c}$	648 A
Strand diameter, d	0.7 mm
Cu:Sc ratio	1.15
Minimum Cu RRR	100
Adjacent contact resistance, R_a	0.5 $\mu\Omega$
Crossing contact resistance, R_c	180 $\mu\Omega$
Twist-pitch, t_p	100 mm
Keystone angle	0.79°
Cable width, w	14.70 mm
Cable mid-thickness, t	1.25 mm
n -value	40

The 11 T cable is modelled as the parallel of 40 strands. Each strand is represented by means of a thermal and an electric component. An additional thermal component represents the epoxy resin composite. Because of the impregnation, heat exchange to the helium is not relevant in the time scales of interest. As a result, the model consists of 40 electric elements, representing the 40 strands, plus 41 thermal elements for the strands plus the insulation. In this paper, we refer to specific strands with an s followed by an index (up to $N = 40$), e.g. $s1, s2, \dots, s40$. Note that, e.g. $s7$ is adjacent to $s6$ and $s8$, while $s1$ is adjacent to $s40$ and $s2$, and similarly $s40$ is adjacent to $s39$ and $s1$.

The thermal properties of the strands are obtained as a mixture of the Nb_3Sn and copper (Cu) cross section contributions. The critical current of Nb_3Sn is defined using the parameterization in [43] and current sharing with the resistive copper matrix takes into account the temperature and field dependence of both critical current and copper resistivity.

Bronze is usually a by-product of the heat treatment process, a residual in the formation of the superconducting A15 Nb_3Sn phase. However, the relative amount of bronze formed in the internal tin process of the strands for the 11 T dipole is rather negligible, namely $< 10\%$ over the cross section. In addition, the much higher electrical resistivity of bronze compared to copper does not make it a relevant component for current sharing and stabilization. For these reasons, the presence of bronze was discarded from the model, and the corresponding cross section ascribed to Nb_3Sn .

The analyses discussed here correspond to a simulation over a 0.3 m domain, namely three twist-pitches. The reason for selecting this limited length was to achieve a high spatial resolution by dense domain meshing, thus studying the electrical phenomena taking place at a short scale around the breakage while keeping the computation time acceptable (a few hours). Results in Section 4 and 5 will show that such a short length already allows grasping the relevant phenomenology of the current distribution in the cable for the pair of boundary conditions analysed.

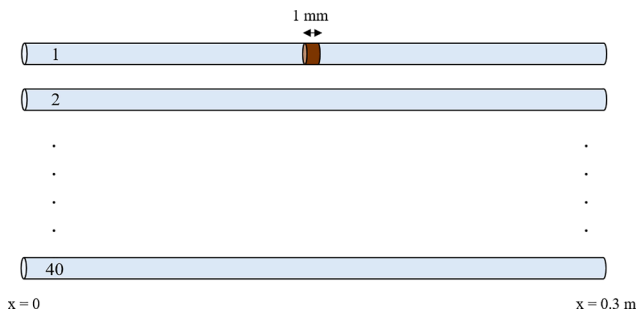


Fig. 1. Schematics of the 40-strand model for the Rutherford cable of the 11 T dipole. A 1 mm broken region (depicted in brown) is located at the centre of strand no.1. Strands are represented as narrow cylinders, but they are treated as 1-D lines by the code.

Fig. 1 presents a schematics of the model. A 1 mm broken region is located at the centre of $s1$, where longitudinal electrical properties are modified to represent the discontinuity. Superconducting properties (J_c, T_c, T_{cs}) are set to zero in the simulated damaged portion of $s1$, while the electrical resistivity of copper, η_{Cu} is set to a factor 1000 higher than its true value. As a result, the longitudinal resistivity is very large, which allows negligible current to flow in the broken region.

3.1. Magnetic field non-uniformity

Strands experience a field variation as they move alternatively between the inner and the outer radius of a coil, due to twisting in Rutherford cables. The field variation also depends on the cable location in the coil. Taking as reference the cable located at the magnet mid-plane, inner layer, and a transport current set to its nominal value of 11.85 kA, the magnetic flux density varies from 11.0 T at the inner radius of the magnet, to 3.5 T at the outer radius of the inner layer (values obtained from ROXIE [54]). We have assumed for simplicity that the field is proportional to the operating current, neglecting non-linear effects such as saturation of the iron yoke. Also, the field variation between the two extremes along the path of a strand has been modelled using piecewise straight lines. Fig. 2 shows the resulting field profile along a few strands.

3.2. Boundary conditions

We have experimented on the effect of electrical boundary conditions, as discussed later. The boundary conditions taken for the nominal case are of uniform current distribution among all strands at the cable ends:

$$I_{b,left}(t) = I_{b,right}(t) = \frac{I_{cable,tot}(t)}{N} \quad (4)$$

The subscript b refers to either the left or the right boundary. $I_{cable,tot}$ is the total transport current in the cable, function of time; N is the number of strands in the cable. This is equivalent to attaching the strands at the boundary to ideal current generators.

We would like to stress here the fact that this is an ideal condition, which cannot be achieved in practice because of the inductive drive discussed in the introduction. This constitutes a limit case useful to grasp the phenomenology of the joint behaviour. As we will discuss also later, it is a convenient assumption looking at local phenomena taking place at short length scales around the breakage, as long as the boundary itself

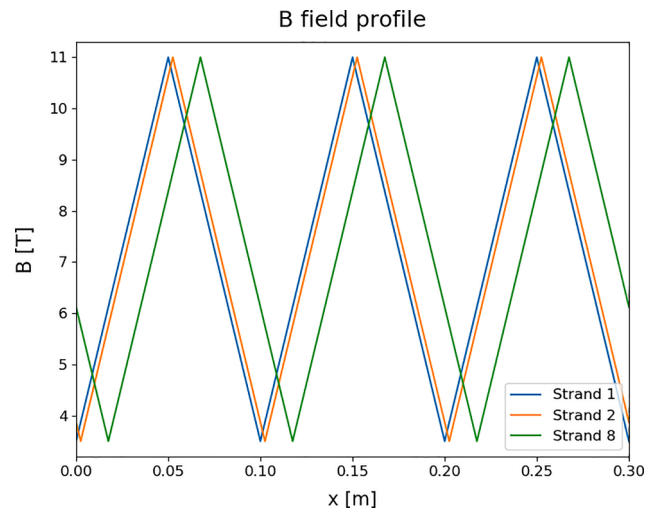


Fig. 2. Field oscillation for a few strands in the Rutherford cable lying on the mid-plane of the 11 T dipole (variation is assumed to be straight). Extreme values are 3.5 T and 11.0 T with a period of 0.1 m, corresponding to the cable twist-pitch.

does not drive the current distribution at the defect location. The other limit case is that of equipotential boundary conditions, equivalent to short-circuited strands at the cable ends, which will be also analysed later in the discussion.

4. Simulation results

4.1. Current overload

For our study of the current evolution in the cable strands, we have taken a reference current ramp starting from zero current, increasing at a constant rate $dI/dt = 10$ A/s, and reaching steady state at 12 kA and $t = 1200$ s. This is followed by a constant current plateau till $t = 1400$ s. This simple ramp is only a part of the more complex electromagnetic cycle experienced by an 11 T dipole in operation, whose nominal current is 11.85 kA, but it is nonetheless representative in terms of current swing and ramp-rate.

We consider first the case of 40 identical wires (i.e. no damage). In this case, the strands are all equivalent to each other in an ideal Rutherford cable, consistent with the mathematical description presented in Section 2.1. The simulation shows that in this case the current sharing is the same in all strands during the ramp, and the current distribution is uniform over the strand length, with each strand ending up with 300 A as expected. Let us recall (Table 1) that the critical current of a strand (1.9 K, 11.0 T) is 648 A.

The results of the case of a broken strand located at the centre of $s1$ are shown in Figs. 3a, 3b, 3c. One can distinguish three groups of strands, where strands of a same group share the same current evolution. The first is the broken strand itself ($s1$, in this case), the second group is formed by the two strands adjacent to the broken one ($s2$ and $s40$), while the third group is the rest of the cable consisting of 37 crossing strands ($s3 - s39$).

Figs. 3a, 3b, 3c report the current distribution in each group of strands, at selected moments in time: $t = 0$ s, 10 s, 1000 s, 1200 s, 1400 s. All strand currents start from zero (the flat, blue lines for $t = 0$ s), and are pushed upwards by the boundary conditions, where the current ramp is imposed in our simulation.

The high copper resistivity in the damaged region of $s1$ does not allow current to flow at the breakage location (in the following, we refer to such location as x_{break}). This is why the current in the broken wire acquires a 'V'-shaped profile, with a linear distribution throughout the ramp, suggesting that the duration of the ramp is much longer than the current redistribution times, see also Section 4.4. Current profiles at the end of the plateau, $t = 1400$ s, are the same as at the ramp end, $t = 1200$

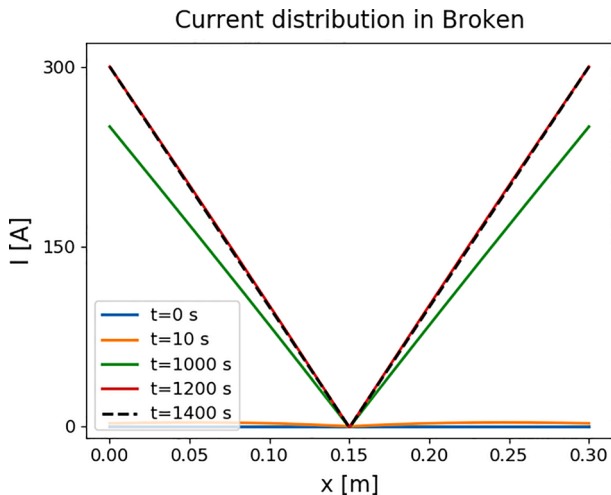


Fig. 3a. Current as $I = I(x)$, with time as a parameter ($t = 0$ s, 10 s, 1000 s, 1200 s, 1400 s), in the broken strand during current ramp and plateau.

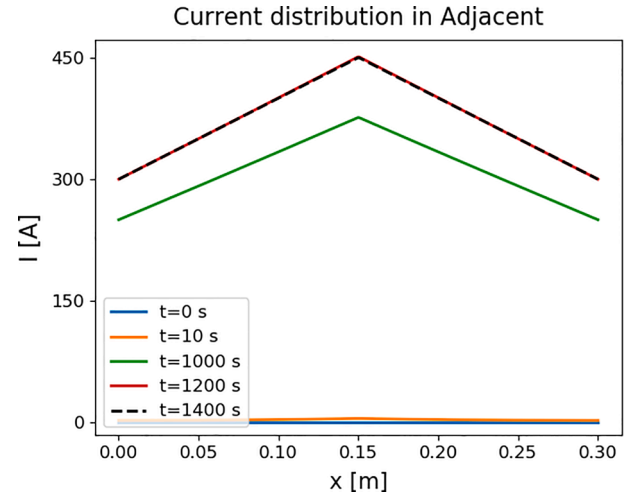


Fig. 3b. Current as $I = I(x)$, with time as a parameter ($t = 0$ s, 10 s, 1000 s, 1200 s, 1400 s), in the adjacent strands during current ramp and plateau.

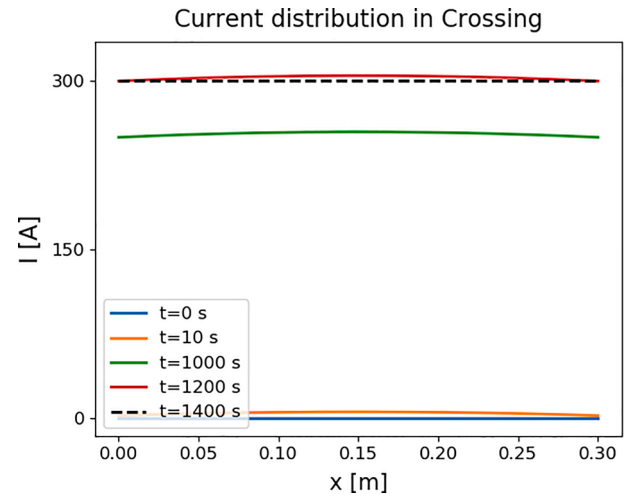


Fig. 3c. Current as $I = I(x)$, with time as a parameter ($t = 0$ s, 10 s, 1000 s, 1200 s, 1400 s), in the crossing strands during current ramp and plateau. Note scale varies from Fig. 3a to Fig. 3c.

s, i.e. the current redistribution is negligible during plateau, consistent with the above observation.

The current distribution in the adjacent strands reflects the current sharing from $s1$. The profile is 'A'-shaped and the current is the highest at x_{break} , reaching 450 A at the ramp end. The peak current of 450 A in the adjacent strands is 50 % higher than expected at the nominal working conditions, for a uniform cable. We observe that the current from the broken strand splits to the two adjacent strands in equal parts. The current transfer from the broken to the adjacent strands takes place over the complete length of the domain, which explains the linear distribution of current also in the adjacent strands.

Finally, crossing strands follow an 'ideal' current evolution, i.e. they behave as if no broken region was present in the cable. Indeed, the current distribution is uniform over the domain both during ramp and plateau, ending up with 300 A. In essence, crossing strands do not take part in the redistribution process.

We shall refer to this phenomenon in the following, as the 'current overload' in strands adjacent to a damaged region. The implication is profound, as shown in the next section. Though it may appear surprising that the current sharing from a broken strand is not uniform in the cable, as would be naively expected, this feature was already postulated and

observed in previous experimental works [7,8]. The results reported in the quoted references apply to the current distribution for a six-twisted strand cable subjected to a step current increase, or as an alternative to selective quench of cable strands. The effect of a quench in one strand was to transfer almost its whole current to the adjacent strands, greatly reducing the maximum current capacity of the cable.

Similar efforts were conducted in [56,57] on bundle of Nb_3Sn filaments and strands subjected to uniform bending. They showed that, a high local strain leads to strong peaking of the local electric field, which causes a significant current transfer between filaments and strands. Other experiments in [34,35] and [36] on CICC agree with these findings.

The question may arise on the influence of boundary conditions. Indeed, the actual boundary conditions of a cable in a coil could be quite dissimilar to the ideal one of prescribed current adopted so far. To investigate this effect, we have taken the other limit case of equipotential boundary conditions, namely of ideal strand short-circuiting at the cable ends (i.e. zero resistance joint).

As stated in Section 3.2 already, these two kinds of boundary conditions constitute the ideal, limit cases. On one side, it is not possible to achieve a uniform injection of current in the strands because of the inductive drive (see the introduction). On the other, one cannot have an equipotential joint, since slight changes in the solder thickness between strands (which is impossible to avoid in practice) result in changes of the inter-strand resistance, and thus in a voltage difference among the strands. These two extreme cases provide bounds for any possible joint behaviour in between.

Figs. 4a, 4b display the current evolution in the broken and adjacent strands in the case of equipotential boundary conditions. In this case, the current in the broken strand is nearly zero at any location along the cable. Only a few amperes circulate in $s1$ during the ramp, due to the inductive effect, then the profile drops to zero at the plateau. Adjacent strands, on the other hand, carry 50 % higher current. As in the case of prescribed current boundary, only the adjacent strands participate to current sharing, demonstrating that the overload phenomenon does not depend on boundary conditions. The difference with respect to the current boundary is that in this case the current overload of the adjacent strands is applied to the whole length of cable. If we transpose this result to the case of a magnet, only a few strands could be carrying excess current originating from a damage location over the whole magnet length.

This corresponds to a decrease of the margin in temperature from 5.6 K, characteristic of the nominal condition, to 3.5 K. With the margins

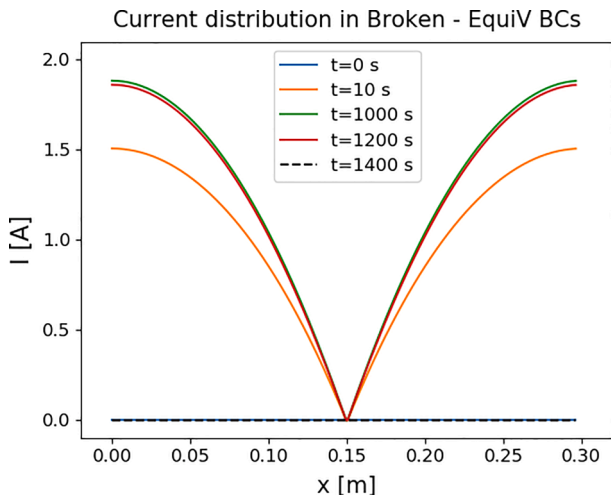


Fig. 4a. Current as $I = I(x)$ with time as a parameter ($t = 0$ s, 10 s, 1000 s, 1200 s, 1400 s) in the broken strand during current ramp and plateau, for equipotential boundary conditions.

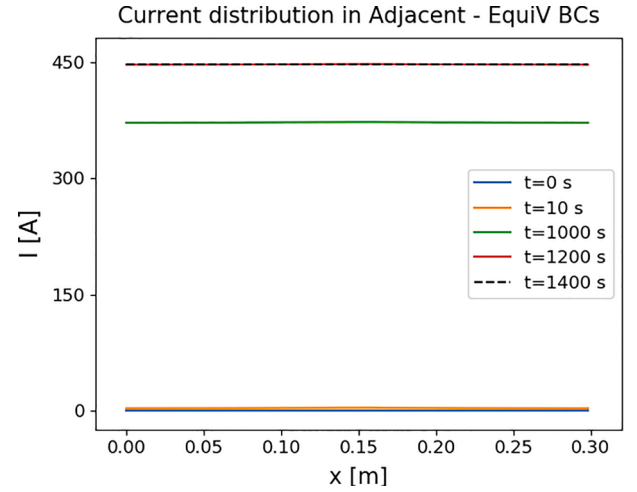


Fig. 4b. Current as $I = I(x)$ with time as a parameter ($t = 0$ s, 10 s, 1000 s, 1200 s, 1400 s) in the adjacent strands during current ramp and plateau, for equipotential boundary conditions.

above, previous calculations have shown that the energy margin in nominal conditions is modest, of the order of 20 mJ/cm³ for fast perturbations, and 70 to 100 mJ/cm³ for steady state power dissipation [30]. These figures scale approximately proportional to the temperature margin.

4.2. Quench cascade

We now progress in complexity, and analyse the case of a current ramp starting from zero current, reaching the cable quench condition. The ramp-rate is set to 10 A/s, as in the previous section.

In the following, we refer to the cable quench current, $I_{quench,cable}$, as the critical current given by the intersection of the magnet loadline with the critical curve. The bore field associated to such current level, $B_{bore,quench}$, is computed assuming a linear increase of the bore field with the increasing current from the nominal operating conditions:

$$B_{bore,quench} = B_{bore,11\ T} \cdot \frac{I_{quench,cable}}{I_{cable,nom}}$$

One finds: $I_{quench} = 14.85$ kA, corresponding to $B_{bore,quench} = 14.3$ T. The current distribution in the initial part of the ramp is identical to what is shown in Figs. 3a, 3b, 3c. Because of the current overload described above, the adjacent strands are those that approach quench conditions first. To examine this phenomenon it is preferable to focus the attention on the current evolution over selected locations of the cable.

Current is extracted at three locations, namely at the domain centre (location of the damage), at the boundary, and in the intermediate position between the two (see Fig. 5). Fig. 6 reports the results for the current evolution at the three selected locations of the adjacent strand. The current at the three locations follows initially a linear increase, driven by the boundary current, with different slopes due to the aforementioned Λ -profile. At approximately $t = 1300$ s we see that the current starts decreasing in the adjacent strands. At this time the peak current in the adjacent strands is 490 A, which corresponds to the critical current at the bore field of 12.9 T and 2.0 K. In such conditions, the strands need to

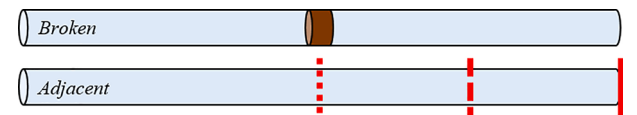


Fig. 5. Model of the broken and of one of the adjacent strands. Current is extracted over three locations of the adjacent strand marked by the vertical red lines (dotted, dashed, solid), and reported as a function of time.

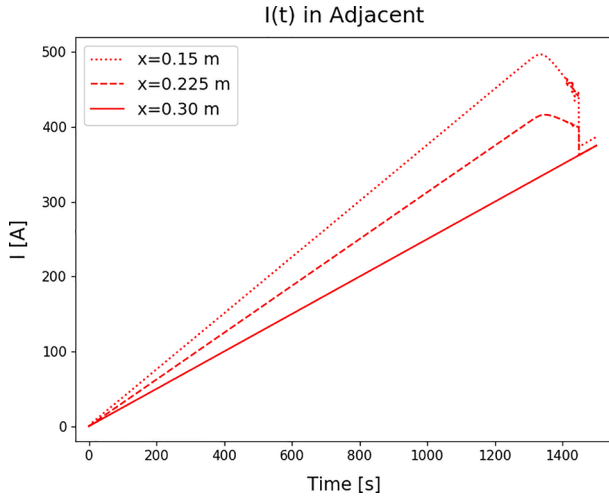


Fig. 6. Current evolution over the three sections of the adjacent strands marked in Fig. 5 (line styles correspond). Profiles split due to the non-uniform Λ -shaped current distribution along the conductor.

redistribute the current. The cable current keeps increasing, as well as the magnetic field, hence the critical current drops further, which causes the decrease in current carried by the adjacent strands observed in the time interval from $t = 1300$ s to $t = 1440$ s. At $t = 1440$ s the current in the adjacent strands drops sharply, finally reaching values very close to the value of the current at the boundary. In fact, at this time the temperature grows rapidly as all strands become normal conducting thus leading to the cable quench, and the current is rapidly distributed uniformly. As a result, $I_{quench, broken} = 14.4$ kA, 450 A below the quench current of the uniform cable.

When the adjacent strands carry a current above the critical one, they develop a voltage and need to transfer the current excess in the rest of the cable. This is shown in Fig. 7, where we focus the attention to the last 300 s of the evolution and plot currents in the adjacent strand s_2 , as well as the first (s_3) and second (s_4) strand neighbouring s_2 . The situation of strands s_{40} , s_{39} and s_{38} is identical.

We notice that at $t = 1320$ s, marked by the vertical black line on the left, the current slope increases in s_3 in response to the decrease in s_2 . The balancing of currents between the two strands takes place on a time scale of a few seconds. At the same time, the slope of the current in s_4 remains unperturbed. This indicates that the current transfer from s_2 takes place only towards its adjacent wire, similarly to the situation described in the previous section. In summary, the quench of a single

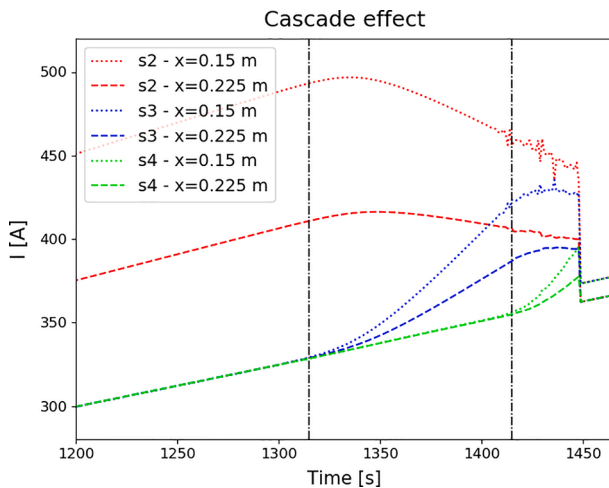


Fig. 7. Accelerated quench cascade.

strand leads to a current overload in the neighbouring strands.

After about 100 s, at $t = 1420$ s, marked by the vertical black line on the right, also s_3 reaches critical current and starts transferring the current excess. This takes place towards s_4 , the only strand available adjacent to s_3 . This is indicated by a switch in the current slopes in s_3 and s_4 , as it occurred previously for s_2 and s_3 . Current sharing and the corresponding transverse heat generation are so high at this stage that this prevents further redistribution and the cable quenches at $t_{quench} = 1440$ s.

We conclude from Fig. 7 that the evolution of current sharing in proximity of quench conditions evolves in a Rutherford cable as a non-linear *accelerated cascade*. Only a small fraction of the cable strands takes part to the current distribution process. For the specific net of electrical properties assumed (R_a, R_c), the rest of the cable strands, despite being affected by the temperature increase, is not taking part in the current redistribution phase.

As a final remark, we note that this quench simulation is representative of a very ideal situation, triggered by an overloaded strand reaching critical current condition and in the absence of any other trigger. Reality is much more complex, but it is evident that any quench mechanism affecting a strand with a current overload caused by a local damage will lead to a similar cascade of successive overloads in the adjacent strands. Because excess current can be in itself a cause of strand instability, the above observation points to the fact that a single strand damage could explain cable performance degradation significantly above the mere percentage of cross section lost to the current carrying capacity. This also depends on the characteristic time and length of the current distribution process, determining whether current transfer from an overloaded strand is effective to unload it over times and lengths characteristic of quench initiation and evolution.

4.3. Voltage current characteristics

In the discussion above, we have focussed on the ‘microscopic’ features of the current distribution process. It is interesting to look also at any effect visible on the voltage-current characteristics at the terminals of the cable. This situation, i.e. considering the cable as a black box and isolating the resistive component of the voltage over the entire conductor length, is akin to measurements as they can be performed in cables. The above case of a current ramp-up is analysed, plotting the $V(I)$ evolution up to quench.

We report in Fig. 8 the results that would be obtained for an intact cable, i.e. with homogeneous properties and no damage. The voltage is very low (off scale) up to ~ 14 kA, and only approaching the critical surface, the sharing to the copper starts building up the voltage signal until quench. The result is the steep transition at the nominal I_c of 14.85

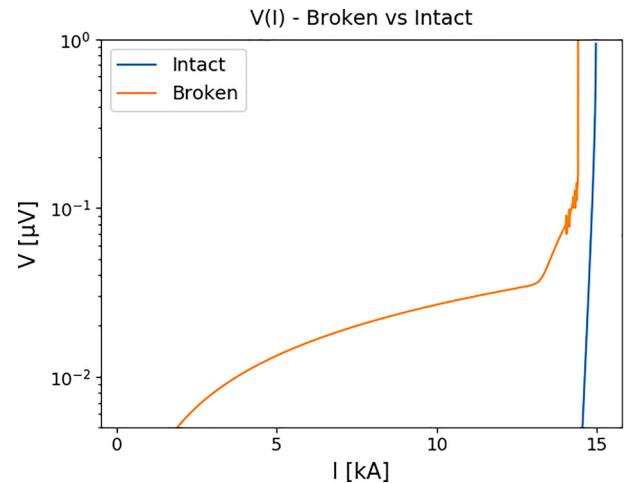


Fig. 8. $V(I)$ characteristics in the broken and intact cables.

kA. This result can be compared in Fig. 8 to the same curve as is obtained for a cable presenting a broken strand. Slopes are representative of the equivalent resistance of the cable.

A low, but non-negligible voltage is observed even at low cable currents. This is due to the current transfer that takes place among the strands $s1$, $s2$ and $s40$ from the very beginning. On the scale of the length and conditions analysed, this behaviour does not compromise cable operation, because heating is small, below 1 mW/m, and can be sustained in the simulation. As the quench cascade initiates, the voltage slope increases, and the transition is softened until the voltage can no longer be sustained and the quench current is reached. As we mentioned earlier, I_{quench} is reduced from 14.85 kA to 14.4 kA.

4.4. Characteristic times and lengths of current distribution

4.4.1. Theory

Strands are twisted in Rutherford cables to ensure transposition and thus reduce the induced current and losses when exposed to a time-varying external magnetic field. Twisting generates a multiplicity of adjacent and crossing contacts among strands, such that the total number of contacts is already in the number of a few thousands in a few twist pitches of cable, a few tens of centimetres.

During a transient, as for example a ramp of the magnetic field, the induced currents flow in all loops formed by the strand contacts to oppose the variation of the magnetic flux (Faraday's law). Such loops extend from half a twist-pitch [9] up to the entire cable length, as confirmed experimentally in [13].

Time constants for the current decay are associated with each loop. For instance, a two-wire system [9] is characterised by an infinite number of components, deriving from one fundamental mode. The solution of the diffusion equation in such a case is:

$$I(x, t) = \sum_{k=1}^{\infty} b_k \left(1 - e^{-\frac{t}{\tau_k}} \right) \sin\left(\frac{\pi k x}{L}\right), \quad (5)$$

where $\tau_k = \tau/k^2$ (k integer). The fundamental mode τ depends on the cable inductance l , conductance g , and on the square of the system length, L [9]:

$$\tau = \frac{l \cdot g \cdot L^2}{\pi^2} \quad (6)$$

assuming a uniform inductance and conductance per unit length between the two strands. The coefficients b_k in Eq. (5) are the Fourier coefficients that determine the steady-state current distribution [13,14].

An N -strand Rutherford cable is actually characterized by an entire set, or *spectrum*, of fundamental modes, whose number is equal to the number of strands [31]. Fig. 9 reports such a spectrum for the 0.3 m, 40-strand Nb_3Sn Rutherford cable for the 11 T dipole analysed earlier.

Values span from 30 ms of mode no.1 (the left-most value), up to 14.4 s of mode no.40. As expected because of symmetry reasons, modes in Fig. 9 are organised in 19 pairs of equal values and 2 spare values, the first and the last [31].

4.4.2. Simulations

The long time scales typical of the ramp-up cases presented above (in the order of 10^3 s for ramp rates of a few tens of ampere/second) are much larger than any of the spectrum modes in Fig. 9, which supports our considerations of quasi steady-state current profiles. Such simulation conditions are too slow to produce a meaningful representation of all modes but the steady state one. To test the modes computed analytically with the numerical model in THEA we introduce a different type of excitation, resembling an impulse. In particular, we induce an *instantaneous* event in the cable, namely a strand breakage occurring at a cable current of 12 kA, starting with an even current distribution among strands (300 A/strand, as seen above). The breakage occurs at $t = 0$ s and the current immediately starts avoiding the damaged spot at x_{break} .

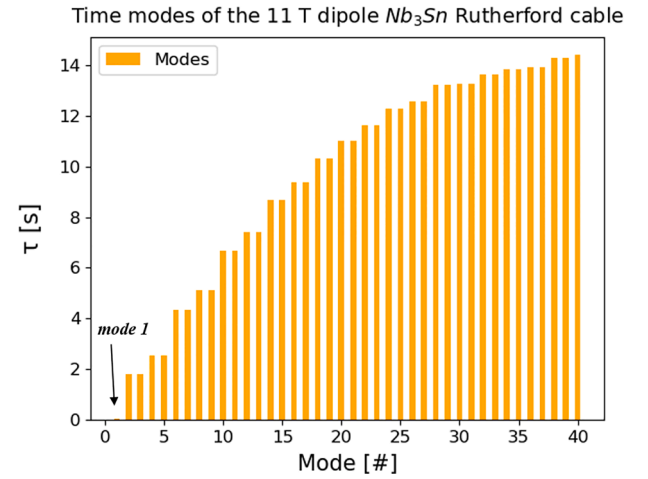


Fig. 9. Spectrum of modes for the 40-strand Nb_3Sn Rutherford cable ($L = 0.3$ m) for the 11 T dipole.

Figs. 10a, 10b display the subsequent evolution both in the broken strand and in the two adjacent strands.

The current redistributes to the adjacent strands as soon as the transient starts, it diffuses over time and reaches steady state after $t = 100$ s. Most current during the transient is transferred to the adjacent strands and, eventually, the steady state condition is the same as in the ramp-up scenario (see Fig. 3). The *current overload* in the adjacent strands has a peak current of 450 A at x_{break} , i.e. 50 % of the current of the broken strand. This is consistent with the discussion above that pointed to the fact that whatever the origin of a reduction of the current carrying capacity of a given strand, redistribution only takes place towards the adjacent ones.

In fact, the current evolution at a specific distance from the breakage is the superposition of modes of each strand, each generating a diffusion-like profile from Eqs.(5) and (6). For an arbitrary excitation, it is not possible to separate the strand modes from each other. However, in the case of the impulse we introduced, at a certain time and spatial distance from the source (the breakage) only a few modes have dominating amplitude. As time advances and distance increases, these modes reduce in amplitude and leave dominance to other modes. Because the simulation yields a current profile that contains this convolution of modes, we prefer to refer to *characteristic times* and *characteristic lengths*, evaluated as follows.

In order to define a characteristic length, we take the current distribution profile at a certain time (e.g. $t = 1$ s in Fig. 11). We then draw a tangent line to the profile of the current originating at the value of the current in the domain centre $I(x_{break})$. The characteristic length is the distance between x_{break} and the intersect of the tangent with the initial value, equal to the boundary current. At a time $t = 1$ s we have hence determined the characteristic length $\lambda_c(t)$, which is representative of the current distribution length at that time.

Conversely, to derive the characteristic time τ_c we take the time evolution of the current at a given location x . The current evolves at this location from its initial value at $t = 0$ s towards an asymptote. We draw a tangent to the current waveform and define the characteristic time from the intersection of this line with the asymptotic value at the given location in space. This allows to establish the time τ_c which is characteristic of current distribution over a length x .

The above procedure can be repeated over a set of times (for $\lambda_c(t)$) and space locations (for $\tau_c(x)$), and the result are the plots shown in Figs. 12a, 12b. We report there the characteristic times and lengths evaluated for a 0.3 m domain, as well as a 1 m domain simulated with the same model (breakage at $x = 0.5$ m).

We first remark that in the log-log plot of Fig. 12 the dependencies $\lambda_c(t)$ and $\tau_c(x)$ are with good approximation power law exponents $1/2$ and

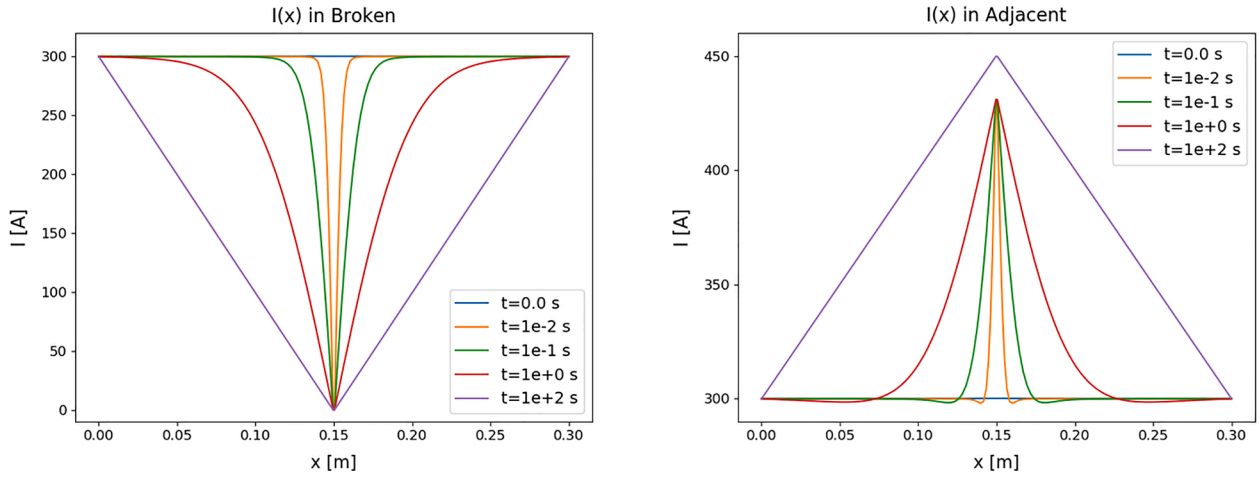


Fig. 10. a, b. Current redistribution in $s1$ and $s2$ ($s40$) after a sudden breakage taking place in $s1$. Note: y-axis scale is not the same in the two plots.

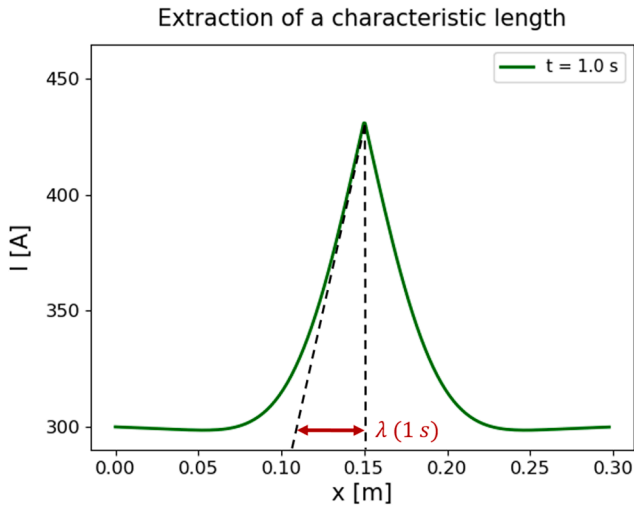


Fig. 11. Extraction of the characteristic length in one of the adjacent strands, at $t = 1$ s after strand breakage in $s1$.

2 respectively. This is the expected dependency, consistent with Eq.(6). We can also note that the characteristic time for a distance of 10 cm is about 12 s. At this length, which is comparable to the domain analysed, we expect the dominant mode to be the slowest one, and the result

obtained is indeed compatible with the slowest mode computed analytically of 14.4 s in Fig. 9. Finally, a characteristic time of 30 ms, the fastest of the modes computed analytically in Fig. 9, corresponds to a distance of a few millimetres from the breakage, compatible with the origin of the fastest mode related to the small loops formed by neighbouring crossing strands.

Extending the simulation to the case of a 1 m domain (purple line in Fig. 10a and light green line in Fig. 10b) yields results that match with those for a shorter domain, as long as the current distribution originated at the central breakage is not affected by the boundary conditions. We can also remark on the known fact that characteristic times for large lengths become exceedingly long (scaling with the square of the cable length). Until these times are reached, the evolution of the current profile, and the current redistribution phenomena always act as if the cable was infinite. The times in question are order of magnitudes longer than quench initiation and evolution times. This means that time and spatial scales of a local defect, the current overload and the quench cascade described so far based on the analysis of a very short length also apply to the situation of long cables in coils.

5. Conclusion and next steps

In this work we developed a numerical model for a Rutherford cable as used customarily for particle accelerators. The model, based on the code THEA, describes the evolution of the cable current in the strands subjected to a selected range of perturbations. Single strands are treated

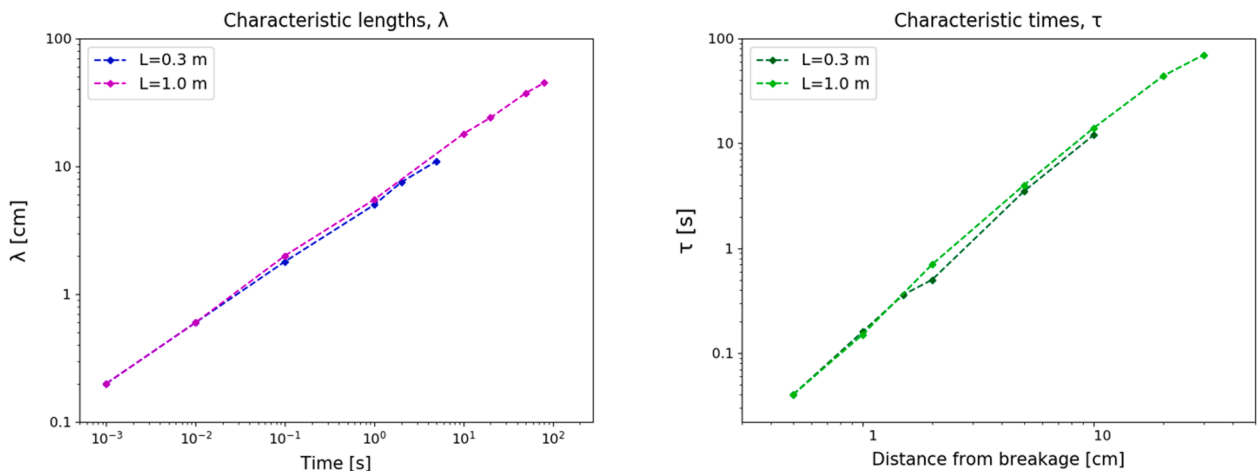


Fig. 12. a, b. Characteristic times and lengths for a 0.3 m and 1.0 m long cables.

as 1-D components, assuming a uniform current and temperature distribution over the strand cross section. The assembly of the individual strands contains 3-D features such as position-dependent conductance and inductance matrices, position-dependent geometry and material properties, and time- and space-dependent magnetic field.

We have specialized the model to the case of the HL-LHC 11 T dipole magnet, and used the model to assess the influence of a localized strand damage. The results reported proved that, given the present set of adjacent and crossing contact resistance values, representative of a Nb_3Sn cable, the preferential path for current sharing from a damaged strand is to the two adjacent strands. This is valid both in steady state and transient, whether in a long or a short cable length, and independently on the situation at the cable boundary (i.e. the joints). The other crossing strands in the cable do not play a significant role in mitigating this current overload of adjacent strands, to the point that their presence can be neglected altogether.

Consequently, the margin to the critical current is considerably reduced. The most overloaded strand, assuming that the damage is at the bore field location, carries nearly 70 % of I_c , to be compared to about 45 % of I_c in nominal conditions. This is true for most of the inner layer, given that the field is approximately uniform at the inner radius of a dipole magnet. In the case of short-circuited strands at the joints (equipotential joints), a strand breakage in any location of the cable would actually expose the adjacent strands to a 50 % higher current along the entire strand length, i.e. eventually also at the bore field location. The above increase of strand current corresponds to a decrease of the margin in temperature, from 5.6 K characteristic of the nominal condition, to 3.5 K.

A second relevant finding, consistent with the idea of current overload explained above, is that the current from a quenching strand is redistributed to the pairs of adjacent strands rather than to all cable strands at the same time. A cable quench in proximity of the critical current hence advances by a cascade of single strand quenches. Depending on characteristic time and length, and operating margin, this poses a limit to the potential for the collective stability of a cable.

Characteristic times and lengths associated to a localized strand damage are typical of diffusion phenomena. They could be computed for N strands from the analytical formulae of [31], and are consistent with the results of numerical simulation. The same behaviour also governs the current sharing among strands when a strand goes normal. In particular, for the conditions considered, the time constants involved in removing the current from the normal strand can be considerably long, such that quench appears as ‘instantaneous’, and current sharing can hardly take place [32–33] and [36].

The findings listed above alert us to the fact that even a localized damage can bear significant consequences on the performance of a magnet. Let us note that the scale of a strand damage can be in the order of millimetres, orders of magnitude shorter than the length of a cable in a coil (e.g. hundreds of meters). We find here an analogy to the problem of stability of superconducting magnets, when comparing the minimum energy to trigger a quench, to the total energy stored in a superconducting magnet [40].

In a next step it will be interesting to use the results and the model to assist magnet performance evaluation. For such exercise one would have to consider in detail conductor and cable parameters (from measurements), as well as the magnet geometry and the distribution of field, stress and strain, all affecting the critical current. Indeed, the results obtained on a short length demonstrate that this level of complexity is manageable, and encourage us towards an extension to the description of a complete magnet length, e.g. approximately 700 m in an 11 T dipole coil. The model could be adapted to other cables and magnets with minor effort.

In such context, one interesting follow-up would be a parametric study on the influence of various key parameters such as contact resistances among strands, which affects the local current redistribution and loss, joints resistance distribution, influencing the current balance at

the connections, as well as the location of damages in the magnet (e.g. high- or low-field regions).

Declaration of Competing Interest

The authors declare that they have no known competing financial interests or personal relationships that could have appeared to influence the work reported in this paper.

Acknowledgements

The present work has been conducted at the Magnets, Superconductors and Cryostats Group of the European laboratory for particle physics (CERN) in Geneva, Switzerland, in the framework of the ‘Volontaires Internationaux’ programme of the French Ministry for Europe and Foreign Affairs (contract no. 0001015078).

G. Succi would like to kindly thank Dr. Alexandre Louzguiti and Dr. Enrico Felcini for the precious support and advices received during the early stage of preparation of this work.

References

- [1] Willering G. 11T Dipole at C-MAC Test Results; 2021. <https://indico.cern.ch/event/1011517/>.
- [2] Haddock C, Kovachev V, Capone D. Measurement of Ramp Rate Sensitivity in Model Dipoles With Ebanol-Coated Cable. IEEE proceedings on particle accelerator conference 1996.
- [3] Haverkamp M. Decay and Snapback in Superconducting Accelerator Magnets. University of Twente; 2003. Ph.D. thesis.
- [4] Ambrosio G, Bauer P, Bottura L, Haverkamp M, Pieloni T, Sanfilippo S, et al. A Scaling Law for the Snapback in Superconducting Accelerator Magnets. IEEE Trans Appl Supercond 2005;15(2):1217–20. <https://doi.org/10.1109/TASC.2005.849535>.
- [5] Turk B. Influence of a transverse conductance on current sharing in a two-layer superconducting cable. Cryogenics 1974;14(8):448–54.
- [6] Ries G. Stability in superconducting multistrand cables. Cryogenics 1980;20.
- [7] Faivre D, Turk B. Current sharing in an insulated multistrand cable in transient and steady current conditions. Applied superconductivity conference 1980.
- [8] Knoopers HG, ten Kate HHJ, van de Klundert LJM. Distribution of Currents in a 6-strand superconducting cable. Proceedings MT-9 1986.
- [9] Akhmetov AA, Devred A, Ogitsu T. Periodicity of crossover currents in a Rutherford-type cable subjected to a time-dependent magnetic field. J Appl Phys 1994.
- [10] Verweij AP. Electrodynamics of Superconducting Cables in Accelerator Magnets. University of Twente; 1995. Ph.D. thesis.
- [11] Verweij AP. CUDE: A model for calculation of electrodynamic and thermal behaviour of superconducting Rutherford cables. Cryogenics 2006;46(7-8):619–26.
- [12] Verweij AP, ten Kate HHJ. Super Coupling Currents in Rutherford Type of Cables due to Longitudinal Non-homogeneities of dB/dt. IEEE Trans Appl Supercond 1995;5(2):404–7. <https://doi.org/10.1109/77.402582>.
- [13] Krempasky L, Schmidt C. Experimental verification of ‘supercurrents’ in superconducting cables exposed to AC-fields. Cryogenics 1999;39(1):23–33.
- [14] Krempasky L, Schmidt C. Ramp-rate limitation in large superconducting magnets due to ‘supercurrents’. Cryogenics 1996;36(6):471–83.
- [15] Krempasky L, Schmidt C. Theory of ‘supercurrents’ and their influence on field quality and stability of superconducting magnets. J Appl Phys 1995;78(9):5800–10. <https://doi.org/10.1063/1.360694>.
- [16] van Lanen EPA, Nijhuis A. JackPot: A novel model to study the influence of current non-uniformity and cabling patterns in cable-in-conduit conductors. Cryogenics 2010;50(3):139–48.
- [17] Nijhuis A, van Lanen EPA, Rolando G. Optimisation of ITER Nb_3Sn CICC for coupling loss, transverse electromagnetic load and axial thermal contraction. Supercond Sci Technol 2012;25.
- [18] Meinecke C, Miri AM, Petranovic R. Numerical Investigation of the Current Distribution in Cable-in-Conduit Conductors Using Lumped Network Models. IEEE Trans Appl Supercond 2001;11(1):2579–82. <https://doi.org/10.1109/77.920395>.
- [19] Bottura L. Modelling stability in superconducting cables. Physica C 1998;310(1-4):316–26.
- [20] Bottura L, Rosso C, Breschi M. A general model for thermal, hydraulic and electric analysis of superconducting cables. Cryogenics 2000;40(8-10):617–26.
- [21] Meinecke C, Miri AM. Coupled electromagnetic and thermal analysis of magnets wound from cable-in-conduit conductors. Physica C 2002;372-376:1427–33.
- [22] Ono M, et al. Estimation Method of Stability for the Multi-strand Superconducting Cables under Partial Current Distribution. IEEE Trans Appl Supercond 1995;5. <https://doi.org/10.1109/77.402613>.
- [23] Mitchell N. Analysis of non-uniform current distribution effects in multistage cable-in-conduit conductors. Cryogenics 1999;39(6):539–56.

- [24] Mitchell N. Modelling of non-uniform current diffusion coupled with thermohydraulic effects in superconducting cables. *Cryogenics* 2000;40(8-10): 637–53.
- [25] Breschi M, Ribani PL. Electromagnetic modeling of the jacket in cable-in-conduit conductors. *IEEE Trans Appl Supercond* 2008;18(1):18–28. <https://doi.org/10.1109/TASC.2008.917565>.
- [26] Breschi M, Granieri PP, Calvi M, Coccoli M, Bottura L. Quench propagation and stability analysis of Rutherford resistive core cables. *Cryogenics* 2006;46(7-8): 606–14.
- [27] Akhmetov A, Bottura L, Breschi M, Ribani PL. A theoretical investigation on current imbalance in flat two-layer superconducting cables. *Cryogenics* 2000;40(8-10):627–35.
- [28] Bottura L, Rosso C. THEA Software 2002. https://supermagnet.sourceforge.io/manuals/Thea_2.4.pdf.
- [29] Bottura L, Breschi M, Musso A. Calculation of interstrand coupling losses in superconducting Rutherford cables with a continuum model. *Cryogenics* 2018;96: 44–52.
- [30] Breschi M, Felcini E, Bottura L. Quench Level of the HL-LHC Nb₃Sn IR quadrupoles. *IEEE Trans Appl Supercond* 2017;27(4):1–5.
- [31] Bottura L, Breschi M, Fabbri M. Analytical solution for the current distribution in multistrand superconducting cables. *J Appl Phys* 2002;92(12):7571–80. <https://doi.org/10.1063/1.1521794>.
- [32] Akhmetov A, Devred A, Mints R, Schermer R. Current Loop Decay in Rutherford-Type Cables. SSCL-Preprint-485 1994.
- [33] Schermer RI, Turck BP. Current sharing between insulated strands in a superconducting cable. ICMC, August 1979 (Madison). https://link.springer.com/chapter/10.1007/978-1-4613-9859-2_71.
- [34] Fevrier A, Hlasnik I, Kokavec L, Poullange JP. Internal Report Saclay, SEDAP/73-124; 1973.
- [35] Turck B. Current redistribution in cables made of insulated, soldered, or oxidized strands. Internal Report LASL; 1979.
- [36] Vysotsky V, Funaki K, Takeo M. Current Non-Uniformity in Multistrand Superconducting Cables. Experimental Studies and Influence Stability of Superconducting Magnets. *IEEE Trans Appl Supercond* 2000;10.
- [37] Rossi L, Bruening O. High Luminosity Large Hadron Collider: A description for the European Strategy Preparatory. Group. CERN-ATS-; 2012-236; 2012. <https://cds.cern.ch/record/1471000>.
- [38] Karpinnen M, et al. Design of 11 T Twin-Aperture Nb₃Sn Dipole Demonstrator Magnet for LHC Upgrades. *IEEE Trans Appl Supercond* 2012;22.
- [39] Ferracin P, et al. Development of the MQXF, the Nb₃Sn Low- β Quadrupole for the HiLumi LHC. *IEEE Trans Appl Supercond* 2016;26.
- [40] Wilson MW. Superconducting Magnets. Clarendon Press; 1983.
- [41] Ambrosio G, et al. Measurement of inter-strand contact resistance in epoxy impregnated Nb₃Sn Rutherford cables. *AIP Conf Proc* 2004.
- [42] Otmani R, Devred A, Tixador P. Interstrand and AC-loss measurements on Rutherford-type cables for accelerator magnet applications. *IEEE Trans Appl Supercond* 2001;11(1):2760–3. <https://doi.org/10.1109/77.919635>.
- [43] Godeke A. Performance boundaries in Nb₃Sn superconductors. University of Twente; 2005. Ph.D. thesis.
- [44] Jewell MC, Lee PJ, Larbalestier DC. The Influence of Nb₃Sn strand geometry on filament breakage under bend strain as revealed by metallography. *Supercond Sci Technol* 2003;16(9):1005–11. <https://doi.org/10.1088/0953-2048/16/9/308>.
- [45] Sheth MK, et al. Study of Filament Cracking Under Uniaxial Repeated Loading for ITER TF Strands. *IEEE Trans Appl Supercond* 2012;22. <https://doi.org/10.1109/TASC.2011.2174554>.
- [46] Miyoshi Y, van Lanen EPA, Dhallé MMJ, Nijhuis A. Microscopic Fractures and Transport Degradation in ITER Type Nb₃Sn Strands. *IEEE Trans Appl Supercond* 2010;20.
- [47] Bruzzone P, Stepanov B, Wesche R, Bagnasco M, Cau F, Herzog R, et al. Status report of the SULTAN test facility. *IEEE Trans Appl Supercond* 2010;20(3):455–7. <https://doi.org/10.1109/TASC.2010.2042583>.
- [48] Miyoshi Y, van Lanen EPA, Dhallé MMJ, Nijhuis A. Distinct voltage-current characteristics of Nb₃Sn strands with dispersed and collective crack distributions. *Supercond Sci Technol* 2009;22(8):085009.
- [49] Sanabria C, Lee PJ, Starch W, Pong I, Vostner A, Jewell MC, et al. Evidence that filament fracture occurs in an ITER toroidal field conductor after cyclic Lorentz force loading in SULTAN. *Supercond Sci Technol* 2012;25(7):075007.
- [50] Devred A, et al. Status of ITER Conductor Development and Production. *IEEE Trans Appl Supercond* 2012;22. <https://doi.org/10.1109/TASC.2012.2182980>.
- [51] Mitchell N, Breschi M, Tronza V. The use of Nb₃Sn in fusion: lessons learned from the ITER production including options for management of performance degradation. *Supercond Sci Technol* 2020;33(5):054007.
- [52] Muzzi L, De Marzi G, Di Zenobio A, della Corte A. Cable-in-conduit conductors: lessons from the recent past for future developments with low and high temperature superconductors. *Supercond Sci Technol* 2015;28(5):053001.
- [53] Bottura L. CID (Cable Interactive Designer) Software. CryoSoft suite; 1998. https://supermagnet.sourceforge.io/manuals/Cid_1.0.pdf.
- [54] Russenschuck S, Auchmann B. ROXIE Software; 1999.
- [55] Keijzer R, Succi G, Willering G, Bordini B, Bottura L, Mangiarotti F, et al. Modelling V-I Measurements of Nb₃Sn Accelerator Magnets with Conductor Degradation. *IEEE Trans Appl Supercond* 2022;32(6):1–5.
- [56] Ciazynski D, Torre A, Li S, Lenoir G. Coupled Mechanical and Electrical Modeling of Nb₃Sn Strand Critical Current Under Bending. *IEEE Trans Appl Supercond* 2016; 26(3):1–6.
- [57] Ciazynski D, Torre A. Analytical formulae for computing the critical current of a Nb₃Sn strand under bending. *Supercond Sci Technol* 2010;23. <https://doi.org/10.1088/0953-2048/23/12/125005>.